The low-order wavefront sensor for the PICTURE-C mission

Christopher B. Mendillo[a], Joshua Brown[a], Jason Martel[a], Glenn A. Howe[a], Kuravi Hewawasam[a], Susanna C. Finn[a], Timothy A. Cook[a], Supriya Chakrabarti[a], Ewan S. Douglas[b], Dimitri Mawet[c], Olivier Guyon[d], Garima Singh[d], Julien Lozi[d], Kerri L. Cahoy[e,f], Anne D. Marinan[e]

[a] Lowell Center for Space Science and Technology, University of Massachusetts Lowell, 600 Suffolk Street 3rd Floor, Lowell, MA 01854, USA;
[b] Astronomy Department, Boston University, 725 Commonwealth Avenue, Boston, MA 02215, USA;
[c] Astronomy Department, California Institute of Technology, Pasadena, CA, 91125, USA;
[d] National Astronomical Observatory of Japan, Subaru Telescope, 650 N A'Ohoku Place, Hilo, HI 96720, USA;
[e] Department of Aeronautics and Astronautics, Massachusetts Institute of Technology, Cambridge, MA, 02139, USA;
[f] Department of Earth and Planetary Science, Massachusetts Institute of Technology, Cambridge, MA, 02139, USA

ABSTRACT

The PICTURE-C mission will fly a 60 cm off-axis unobscured telescope and two high-contrast coronagraphs in successive high-altitude balloon flights with the goal of directly imaging and spectrally characterizing visible scattered light from exozodiacal dust in the interior 1-10 AU of nearby exoplanetary systems. The first flight in 2017 will use a 10^{-4} visible nulling coronagraph (previously flown on the PICTURE sounding rocket) and the second flight in 2019 will use a 10^{-7} vector vortex coronagraph. A low-order wavefront corrector (LOWC) will be used in both flights to remove time-varying aberrations from the coronagraph wavefront. The LOWC actuator is a 76-channel high-stroke deformable mirror packaged on top of a tip-tilt stage. This paper will detail the selection of a complementary high-speed, low-order wavefront sensor (LOWFS) for the mission. The relative performance and feasibility of several LOWFS designs will be compared including the Shack-Hartmann, Lyot LOWFS, and the curvature sensor. To test the different sensors, a model of the time-varying wavefront is constructed using measured pointing data and inertial dynamics models to simulate optical alignment perturbations and surface deformation in the balloon environment.

Keywords: exoplanets, exozodiacal dust, debris disks, balloon, direct imaging, fine pointing, wavefront control, high-contrast imaging

1. INTRODUCTION

Extremely precise optical wavefront sensing and control is required to directly image exoplanets and dust around nearby stars. At inner working angles of less than 2 λ/D in visible light, residual phase errors less than 1 nm RMS and simultaneous amplitude control are required. For space and balloon missions, this control problem is often separated into two parts based on the spatial and temporal scale of the aberrations. A low-order, high-speed system is used to remove large errors induced by telescope pointing and flexing – all of which vary rapidly in time. A high-order, low-speed control system can then be used to perform simultaneous phase and amplitude control on the resulting quasi-static wavefront in order to create a dark zone of extremely high contrast near the star. This work will detail the selection of a low-order wavefront sensor (LOWFS) and control system for the Planetary Imaging Concept Testbed Using a Recoverable Experiment - Coronagraph (PICTURE-C)

Further author information: (Send correspondence to C.B.M.)
C.B.M.: E-mail: christopher.mendillo@gmail.com

Techniques and Instrumentation for Detection of Exoplanets VII, edited by Stuart Shaklan, Proc. of SPIE Vol. 9605
960519 · © 2015 SPIE · CCC code: 0277-786X/15/$18 · doi: 10.1117/12.2188238

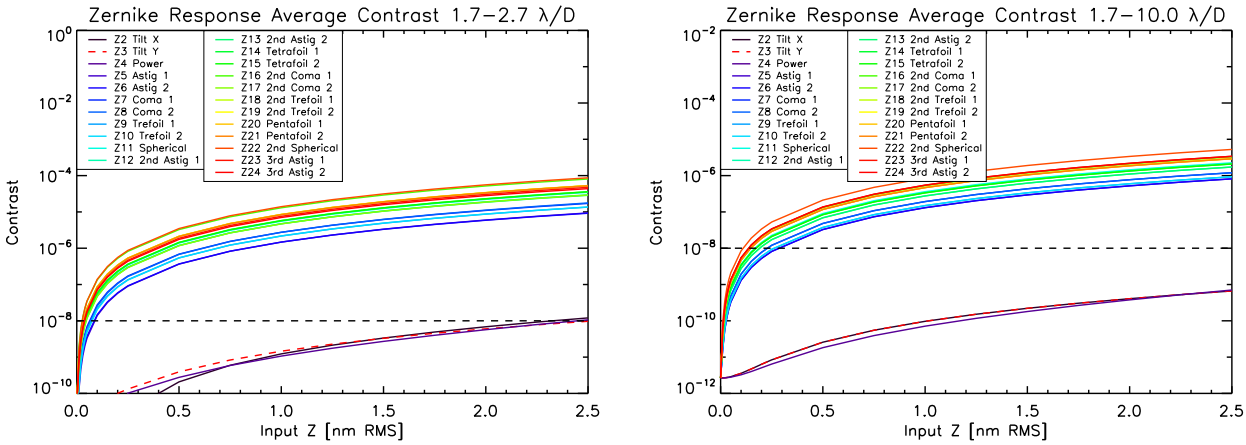

Figure 1: Broadband VVC sensitivity to the first 24 Zernike modes. The Zernike coefficients are RMS normalized. Left: average contrast from 1.7-2.7 λ/D. Right: average contrast from 1.7-10 λ/D.

balloon mission. This mission will fly once in 2017 and again in 2019. The 2019 flight will incorporate a vector vortex coronagraph (VVC) and microwave kinetic inductance detector (MKID) and will achieve a raw contrast of 10^{-7} at 1.7 λ/D. The following sections will examine the sensitivity of the VVC to low-order aberrations and the disturbance environment and resulting low-order errors that are expected in flight. Simulations of several sensors in different configurations within the instrument will be performed to aid the selection of a LOWFS that meets the mission requirements.

2. CORONAGRAPH SENSITIVITY

This work will consider only the VVC instrument to be used in the second PICTURE-C flight since it requires higher performance wavefront control. The instrument will incorporate a charge 4 VVC mask[1] operating in the visible over a 20% band centered at 600 nm (540-660 nm). A 32×32 actuator AOA Xinetics[2] deformable mirror (DM) will be used to control both amplitude and phase in half of the image plane to create a dark zone extending from 1.7-10 λ/D. The simulations presented here were performed using the IDL PROPER library[3] and the VVC model developed for NASA TDEM NNH09ZDA001N.[4,5] A more detailed description of the PROPER simulations can be found in these proceedings (Douglas et al. 9605-44). The mission raw contrast requirement is 10^{-7} averaged over the inner resolution element (1.7-2.7 λ/D) of the dark zone. To provide margin, a design contrast requirement of 10^{-8} is used here.

Figure 1 shows the sensitivity of the VVC to the first 24 Zernike modes. The charge 4 VVC shows low sensitivity to tip, tilt, and focus (Z2-Z4), but is very sensitive to higher order terms (Z5-Z24). Previous simulations of the VVC sensitivity[6] show similar results. The simulations shown here are tailored to the PICTURE-C bandpass and field of view. To achieve 10^{-8} contrast, the residual Zernike coefficients for Z2-Z4 must remain below 2.5 nm RMS and Z5-Z24 must remain between 0.02-0.1 nm RMS.

3. LOW-ORDER ERRORS

3.1 Pointing

The largest source of low-order error is the residual pointing error from the Wallops Arc Second Pointer (WASP) system. WASP is a 2-axis gimbal mount that actively points the science payload. WASP has achieved $< 0.2''$ RMS pitch and yaw control during a number of test flights;[7] however, knowledge of the WASP performance at high frequencies is limited by noise in the onboard gyroscope measurements. High frequency jitter is critical for direct imaging because a limited-bandwidth control system must be used to stabilize the centration of the star on the coronagraph mask at the milliarcsecond (mas) level. Pointing jitter caused by mechanical vibration at frequencies above the control band will pass directly through to the instrument and degrade the performance. The WASP system uses brushless DC motors to drive pitch and yaw control. There are no reaction wheels to

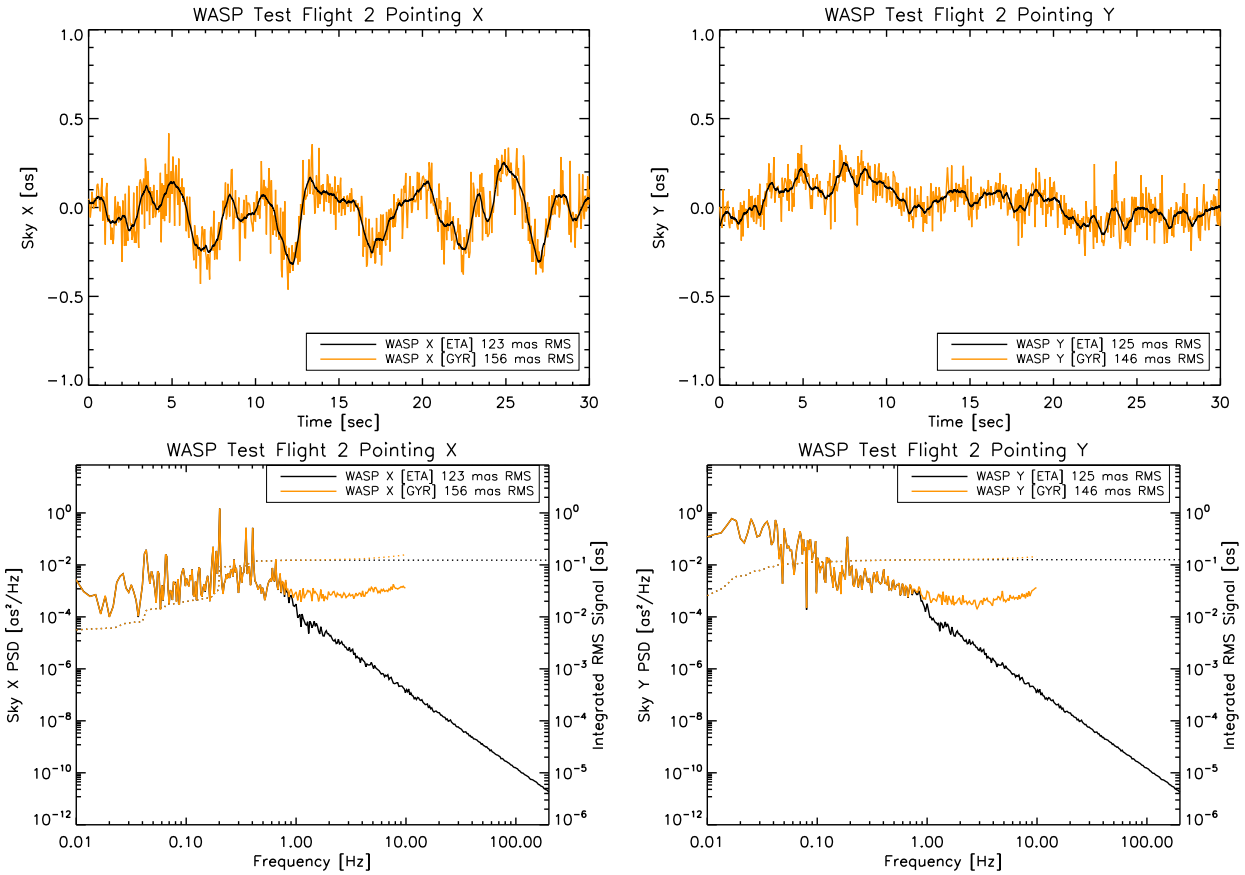

Figure 2: Top: WASP gyroscope pointing data (orange) from the second WASP test flight over a 30 second window. Bottom: The power spectral density of the time-series data. The integrated RMS error is shown as the dotted line and uses the right axis. To remove sensor noise, the estimated true attitude (black) is constructed by mixing gyro data at low frequencies with a power-law falloff at high frequencies below the gyro noise floor.

create high frequency vibration. The DC motors run continuously at 2 Hz and are geared down to 0.04 Hz at the drive shafts. These motors are unlikely to produce any vibration above the control bandwidth – between 5-10 Hz. Pointing data from the second WASP test flight is shown in Figure 2. The raw gyro data cannot be used to simulate the payload pointing because it shows far too much power at high frequencies due to sensor noise. Instead, a model of the estimated true attitude (ETA) is constructed from the gyro data by assuming an f^{-4} power-law falloff at high frequencies below the gyro noise floor. The same approach was taken when analyzing the sounding rocket pointing performance during the first flight of Planetary Imaging Concept Testbed Using a Rocket Experiment (PICTURE) in 2012.[8]

3.2 Pointing Induced M1-M2 Displacement

The WASP pointing induces mechanical flexing of the payload structure. Typical WASP control torques are between 1-4 ft lbs. Finite element analysis (FEA) of the telescope shown in Figure 3 predicts 0.25 μm of secondary mirror decenter per 1 ft lb of torque due to flex of the secondary support structure. An optical model of the telescope is used to determine the resulting Zernike aberrations induced by this misalignment. Finally, WASP torque sensor data from the same time window shown in the previous section is used to produce a time series of Zernike aberrations due to structure flex that are synchronized with the pointing data.

3.3 Gondola Pendulum M1 Gravity Sag

The experiment gondola is suspended below the balloon on a ∼1000 ft cable. Disturbances from air currents in the stratosphere cause the gondola to swing back and forth. The primary pendulum mode of the system has

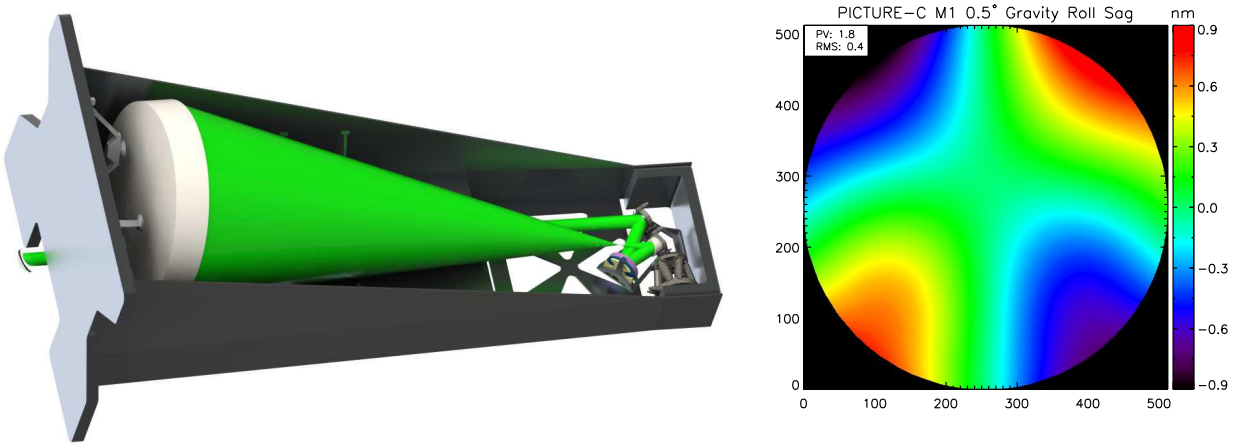

Figure 3: Left: PICTURE-C telescope structure. The WASP system attaches to the mounting plate shown at the far left. Right: Primary mirror sag induced by 0.5° gravity rotation due to gondola pendulum.

a frequency of ∼0.045 Hz (22 second period) and an amplitude of 0.5°. In the telescope reference frame, this swinging motion is perceived as a 0.5° rotation of the local gravity vector, which induces a periodic gravity sag aberration on the primary mirror. FEA of the $24 \times 4''$ solid ultra low expansion (ULE) glass mirror is shown in Figure 3. A simple 3-point mount with 2.5″ RTV-bonded pucks is used in these simulations. The pendulum-induced gravity sag distorts the mirror surface by 1.8 nm PV and 0.4 nm RMS. The aberration is dominated by astigmatism. A time series is created by modulating a 24 Zernike fit to this surface by a 0.045 Hz sine wave.

3.4 Gondola Pendulum M1-M2 Displacement

The pendulum mode discussed in the previous section also displaces the primary mirror relative to the secondary as the mirror mount flexes. This time-varying decenter produces a new set of aberrations on a 22 second period. The same FEA used in the previous section shows the decenter at the maximum gravity rotation is $\sim 0.5\mu$m. An optical model of the system is used to output a set of Zernike coefficients for this decenter, which are then modulated by a 0.045 Hz sine wave to produce a Zernike time series. The full set of time-dependent Zernike errors is plotted in Figure 4.

4. LOW-ORDER SENSING AND CONTROL

4.1 Controller Bandwidth

A simulated ideal LOWFS is used to determine the required low-order wavefront controller (LOWC) bandwidth. This sensor simply uses the known values of each Zernike coefficient in the simulation without adding any measurement noise. The control system is a proportional + integral + differential (PID) servo. The update rate of the control system and the controller gains determine the system bandwidth. The residual WASP pointing error places the most demanding constraint on bandwidth. Figure 5 shows the ideal LOWC operating at 200 Hz and 400 Hz on the Z2 (tip) Zernike with optimized gains. The Z3 (tilt) results are very similar. The residual 1σ Z2 error is 0.52 nm RMS at 200 Hz and 0.23 nm RMS at 400 Hz. Since the coronagraph will see up to 5σ errors, a 400 Hz system is required to keep the combined (RSS) Z2 and Z3 errors below 2.5 nm RMS (see Figure 1).

4.2 LOWFS Options

The optical design of the VVC instrument (Figure 6) provides two locations for the LOWFS. The first is created upstream of the VVC mask by a dichroic beamsplitter. The dichroic transmits blue light shortward of 540 nm to the LOWFS and reflects red light into the coronagraph. Three potential sensors are being considered for this location: a Shack-Hartmann wavefront sensor, a curvature wavefront sensor, and a pyramid wavefront sensor. Only the Shack-Hartmann and curvature sensors are simulated here, the pyramid sensor will be investigated in

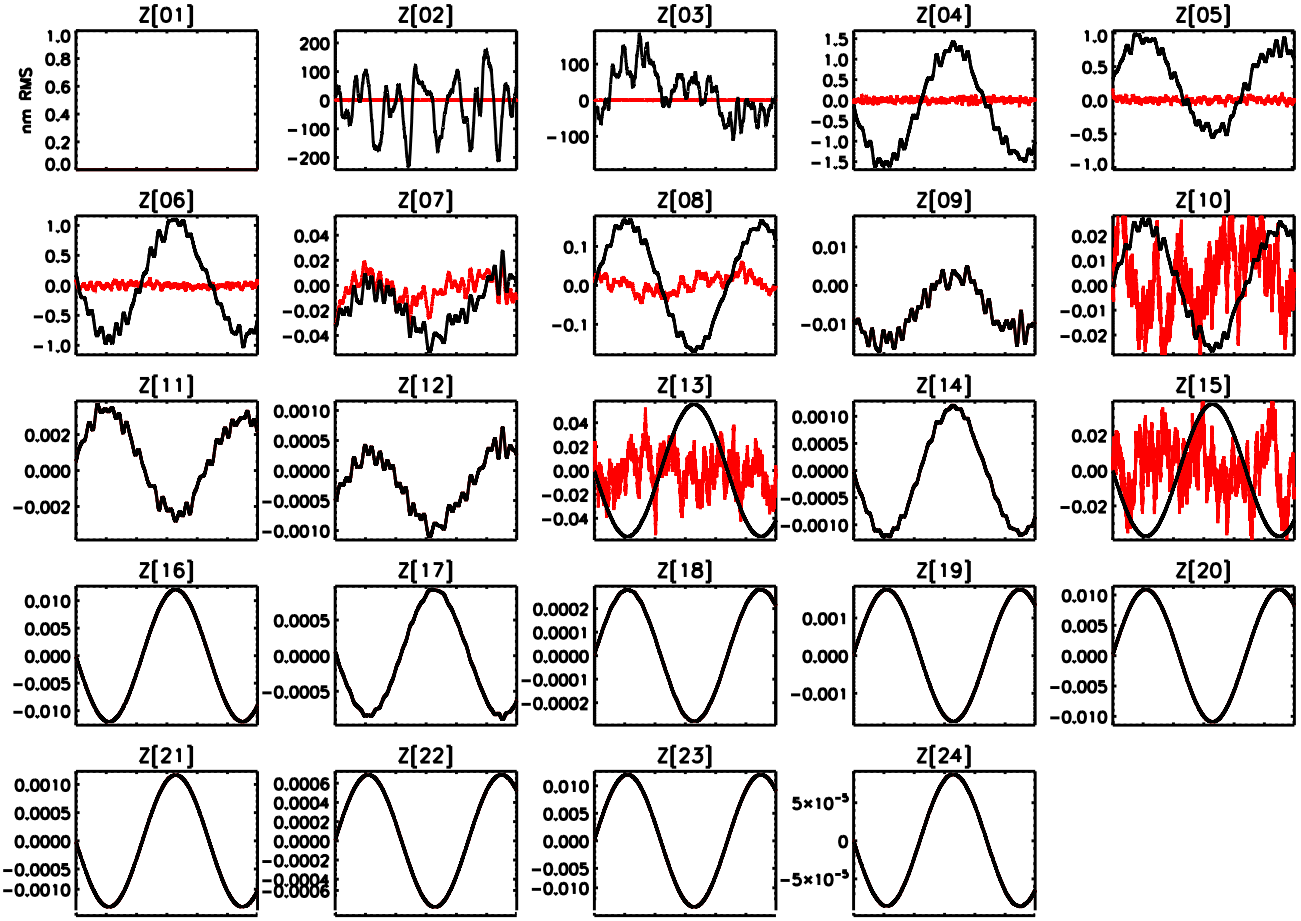

Figure 4: The black lines show the input Zernike coefficients as a function of time (RMS normalized). The plots all show a 30 second window. The red lines show the closed loop performance using a 400 Hz PID control system with the Lyot LOWFS (see Section 4). Zernike errors showing only black lines are insignificant at the 10^{-8} level and are disabled in the control system.

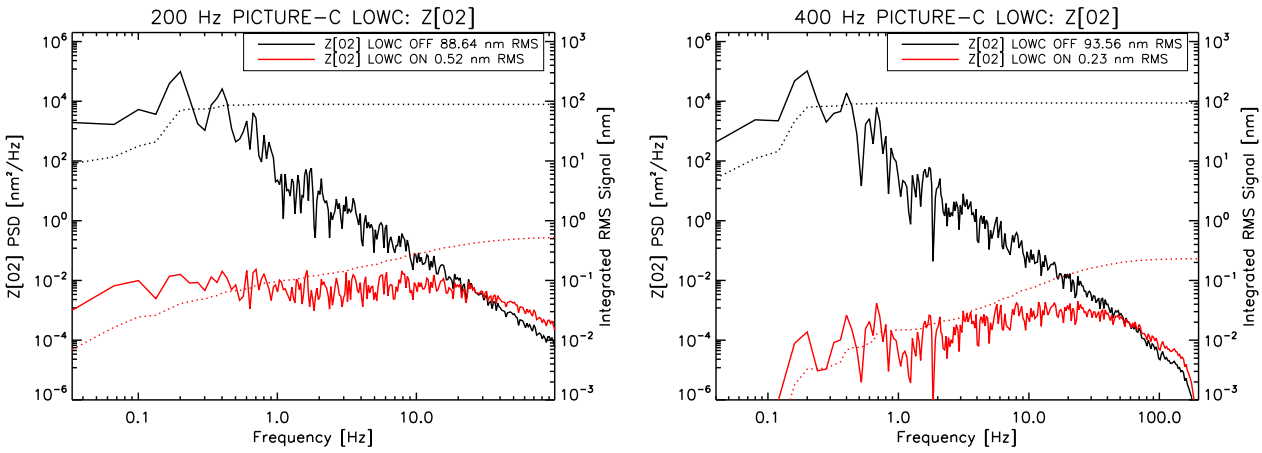

Figure 5: Power spectral density plots showing the closed loop pointing (Z2) performance of a 200 Hz (left) and 400 Hz (right) PID loop using an ideal sensor with no noise. The integrated RMS error is shown as the dotted line and uses the right axis. A 400 Hz loop is required to reach 10^{-8} raw contrast.

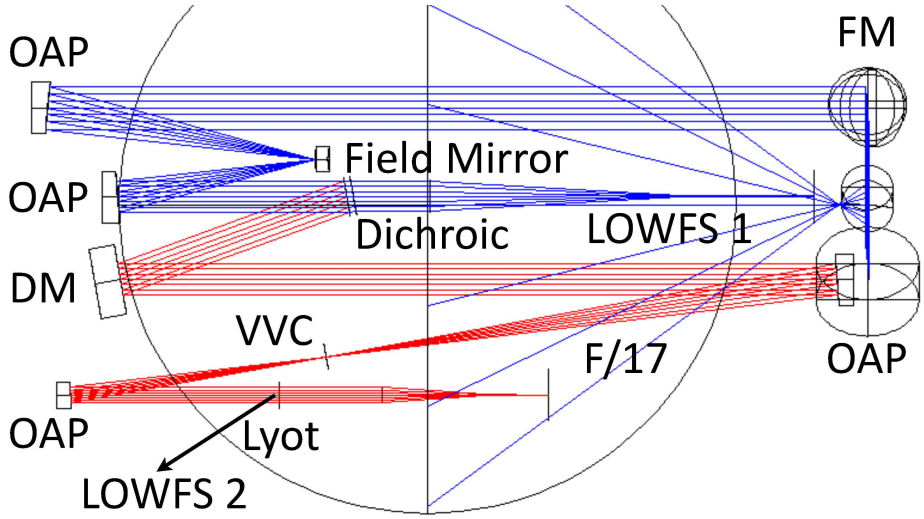

Figure 6: Optical layout for the VVC instrument. The two possible LOWFS locations are shown. The first is located upstream of the coronagraph in the shortpass beam created by a dichroic beamsplitter. The second location is created using a reflective Lyot stop.

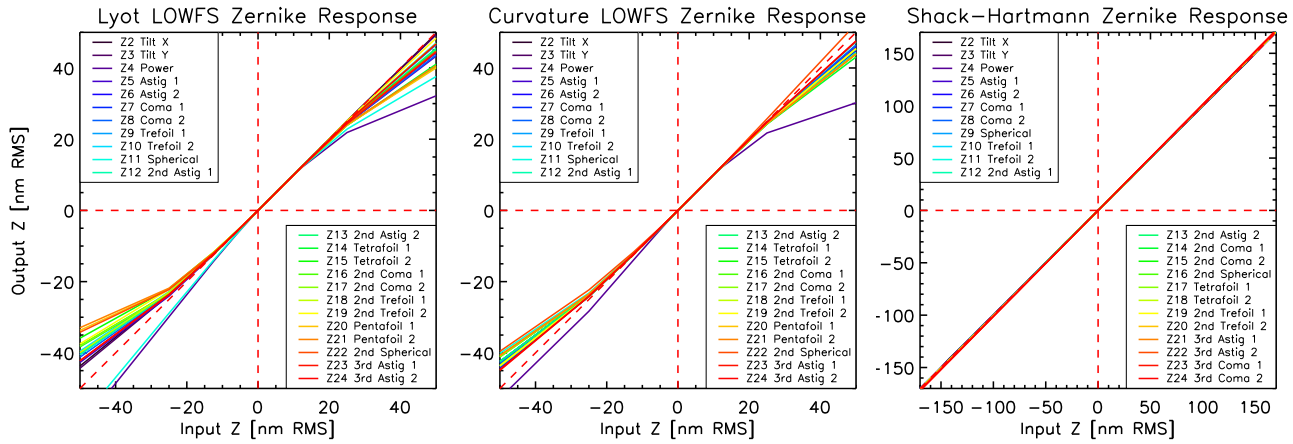

Figure 7: Input vs. output response curves for the three LOWFS options: Lyot (left), curvature (middle), Shack-Hartmann (right). The Shack-Hartmann sensor shows far greater linearity and dynamic range than the other sensors. The Lyot and curvature sensors remain monotonic beyond 50 nm RMS and are able to drive the error terms into the inner ± 10 nm where both are linear.

the future. This location takes advantage of the blue light that would otherwise be lost. It is, however, non-common-band and non-common-path with the coronagraph and will introduce systematic errors in the sensor output.

The Shack-Hartmann sensor simulated here uses a 9×9, 192 μm pitch lenslet array with an 8 mm focal length. A pair of lenses are used to compress the beam down to the array diameter. A modal reconstruction algorithm is used to measure the Zernike terms from the individual spot displacements. In this technique, derivatives of the Zernike polynomials are fit directly to the measured wavefront slopes to recover the Zernike coefficients. This method has proven to be more accurate than zonal techniques like direct integration, Southwell reconstruction and spline fitting – all of which have greater sensitivity to noise and can exhibit strong boundary effects. An example of the Shack-Hartmann modal reconstruction is shown in Figure 8.

The second LOWFS location is created downstream of the VVC mask by using a reflective Lyot stop to pass the light diffracted by the mask to a Lyot-LOWFS (LLOWFS). This location has the benefit of being common-path and common-band with the coronagraph. The reflective Lyot stop is appropriate for transmissive phase mask coronagraphs like the VVC, whereas a reflective coronagraph mask is more suitable for systems where the occulting mask rejects the starlight – such as the band-limited mask[9] or PIAA-based coronagraphs.[10] The LLOWFS has been developed for use on the Subaru Coronagraph Extreme AO (SCExAO)[11] and a similar design is used here.

The operation of the curvature and Lyot sensors is nearly identical. Both use a pair of lenses to form a slightly out-of-focus image of the star on a detector. The detector chosen for these simulations is an e2V CCD39 80×80 chip[12] operating with an Astronomical Research Cameras (ARC) Gen III controller.[13] The CCD full-well limit is 3×10^5 e-/px. The average dark rate is 58×10^3 e-/px/s at room temperature and the read noise is $\sim$12 e-/px RMS. Both sensors operate under the assumption that small changes in the wavefront ($\sim$10 nm) produce a linear response in the intensity pattern of the out-of-focus image. To operate these sensors, first a response matrix is constructed by probing the LOWC actuator with the first 24 Zernike polynomials and recording the response on the detector. The LOWC actuator chosen for PICTURE-C is an AOA Xinetics[2] 76-channel deformable mirror mounted on a tip/tilt stage. The Zernike response images shown in Figure 8 are the difference between the ideal image and the probed image. These images are placed into a matrix and inverted using singular value decomposition (SVD). The resulting inverted matrix can be multiplied by any image to approximate the Zernike error coefficients.[10,11] While the response is not linear for large excursions, it often remains monotonic out to $\sim$100 nm allowing the control system to drive the error back into the linear regime (see Figure 7).

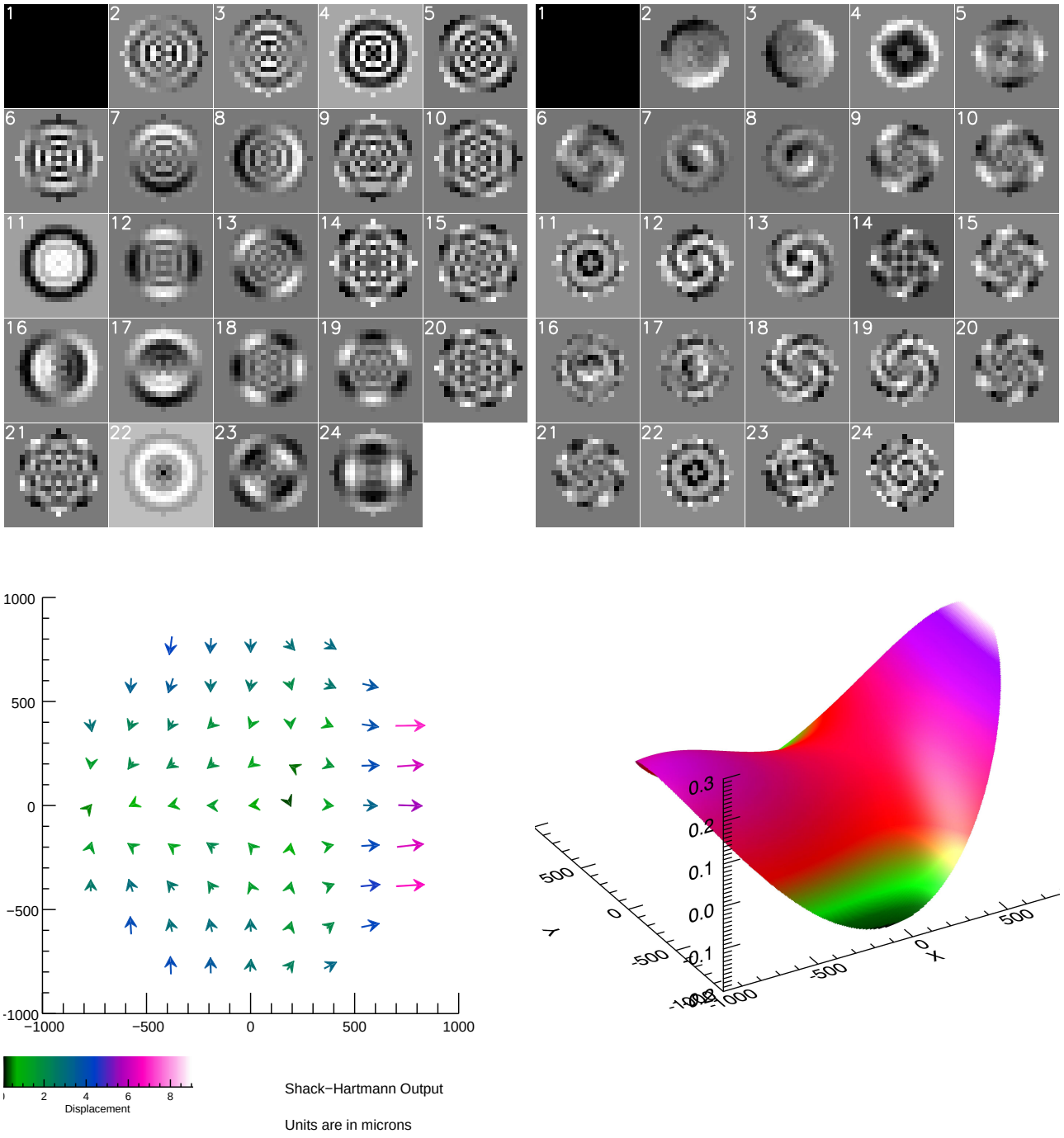

Figure 8: Top: Simulated images showing the curvature (top-left) and Lyot (top-right) sensor response to the first 24 Zernike modes. Bottom: Example Shack-Hartmann spot displacement map (bottom-left) and modal wavefront reconstruction (bottom-right).

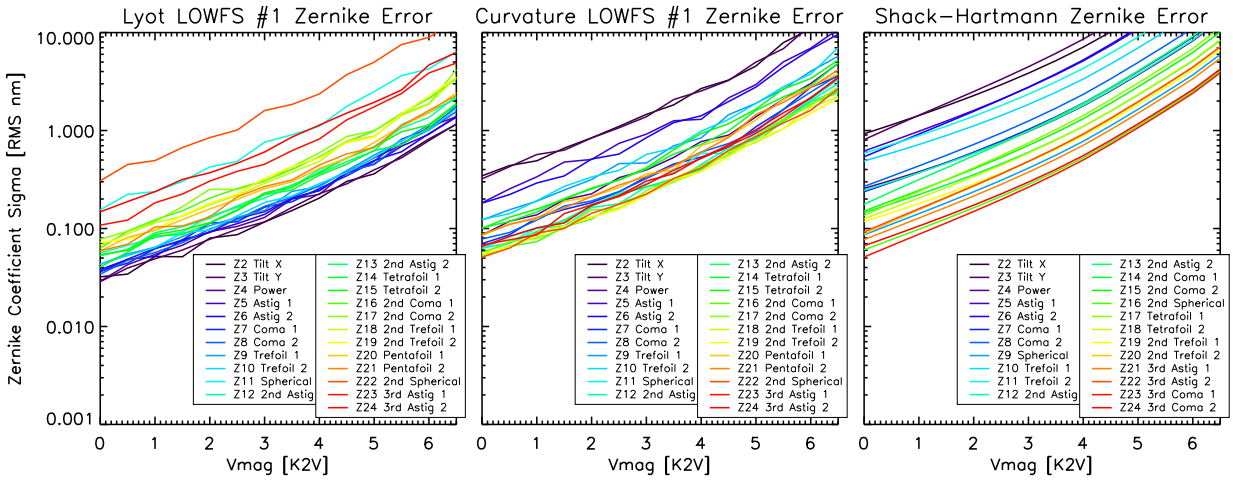

Figure 9: Simulated Zernike measurement uncertainty as a function of stellar brightness for each sensor.

4.3 Sensor Noise

The measurement noise of each sensor is modeled by first calculating the broadband throughput of the optical system at each sensor location. To do this, the metallic coating reflectivities of each mirror, glass transmission of each lens, and detector quantum efficiency are all multiplied together across the operating band of the sensor. Simulated spectra[14] of a K2V star are used to calculate the observed photon count rate at each sensor from stars of varying brightness. Simulated images are constructed that include photon noise, detector read noise and noise from dark counts. A test wavefront is then injected into the system, one for each of the Zernike modes, and hundreds of sensor measurements are made using random variations in the sensor noise to determine the 1σ measurement errors for each Zernike mode as a function of stellar brightness. The results for each sensor are shown in Figure 9. The Lyot sensor shows the lowest noise for the lower-order Zernike modes where most of the system aberrations are found. The curvature sensor makes better use of the blue photons in the LOWFS-1 channel than the Shack-Hartmann sensor, which shows the worst performance.

4.4 Closed Loop Control

The modeled sensor noise is then injected into the control system to simulate closed loop wavefront control operating at 400 Hz. Figure 10 shows the performance of each sensor broken down into each Zernike mode. As a test case, the star ϵ Eri (V=3.73, K2V) is chosen for these simulations. It is one of the dimmest science targets selected for the mission. The sensors are able to control at levels far below their measurement noise by greatly reducing the controller gain for the higher order Zernike modes and disabling modes that do not show strong errors. High gain is required for tip and tilt (pointing), as shown in Section 4.1, but reduced gain (and reduced bandwidth) is allowable for the higher order terms that do not require such aggressive control.

Finally, the end-to-end PROPER model is run to simulate the effect of each sensor on the coronagraph performance. In reality, the LOWC system will operate at rates 10^4 - 10^5 times faster than the high-order electric field conjugation (EFC)[15] control system that creates the dark zone. Given the fact that each end-to-end simulation takes $\sim$10 seconds to run, it is computationally prohibitive to run the full simulation at the cadence of the LOWC. Instead, a statistical approach is taken where the closed-loop residual Zernike errors (Figure 10) are injected into the end-to-end simulation using a random draw from a Gaussian distribution. Five aberrated wavefronts are propagated through the system and averaged into each EFC correction. This is done to simulate the effect of residual low-order errors on the image plane sensing. Figure 12 shows the dark zone convergence with each iteration. As a positive check of our theoretical control limit, the ideal sensor is able to reach contrasts below 10^{-8} in steady state. The Lyot sensor is the only realistic sensor capable of reaching contrasts at or below 10^{-8}. The Lyot LOWFS system shows excursions at the $2-3\times10^{-8}$ level. While these remain below the mission requirement of 10^{-7} with margin, further work can be done to improve the Lyot sensor. The image size on the detector can be reduced to improve the signal-to-noise ratio in each pixel. This comes at the cost of reduced

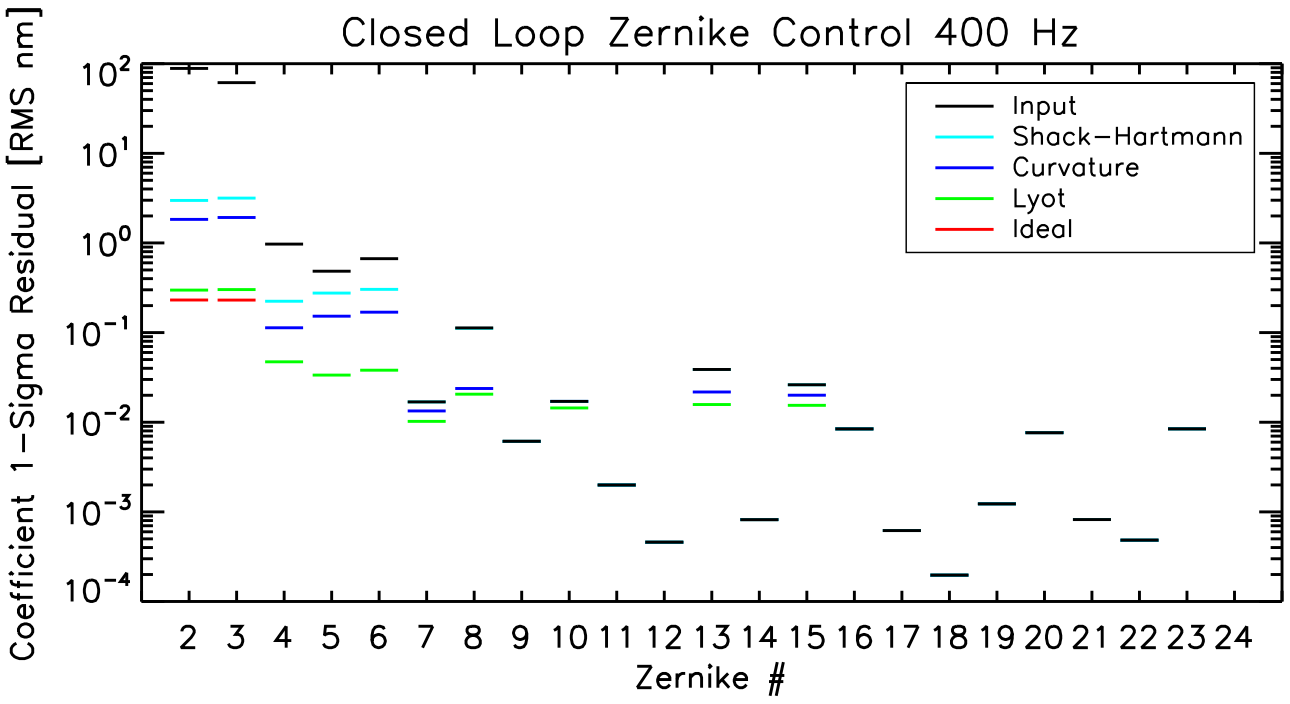

Figure 10: Closed loop performance for each of the sensors on ϵ Eri (V=3.73, K2V). The black lines show the input wavefront error and are the standard deviations of the time series shown in Figure 4. The red lines show the performance of an ideal sensor with no noise. Note: for the higher-order terms, the ideal sensor lines fall below the X-axis. The Lyot LOWFS is the highest performing sensor for all Zernike modes. Zernike errors showing only black lines are insignificant at the 10^{-8} level and are disabled in the control system. The Shack-Hartmann sensor is disabled for modes above #6 due to its high noise level.

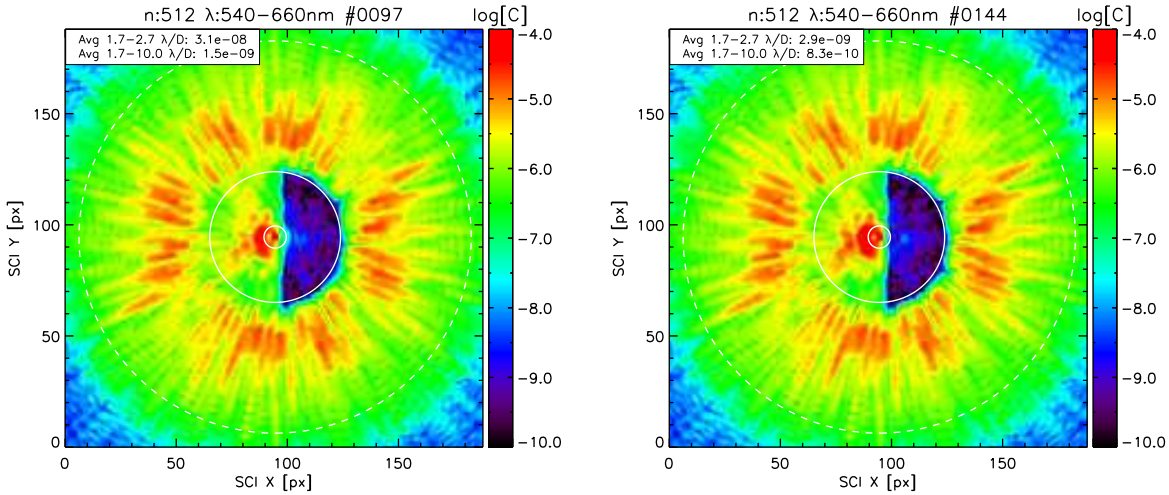

Figure 11: Example contrast maps from the Lyot-based LOWC. These maps correspond to iteration #97 (left) and #144 (right) from the Lyot plot in Figure 12.

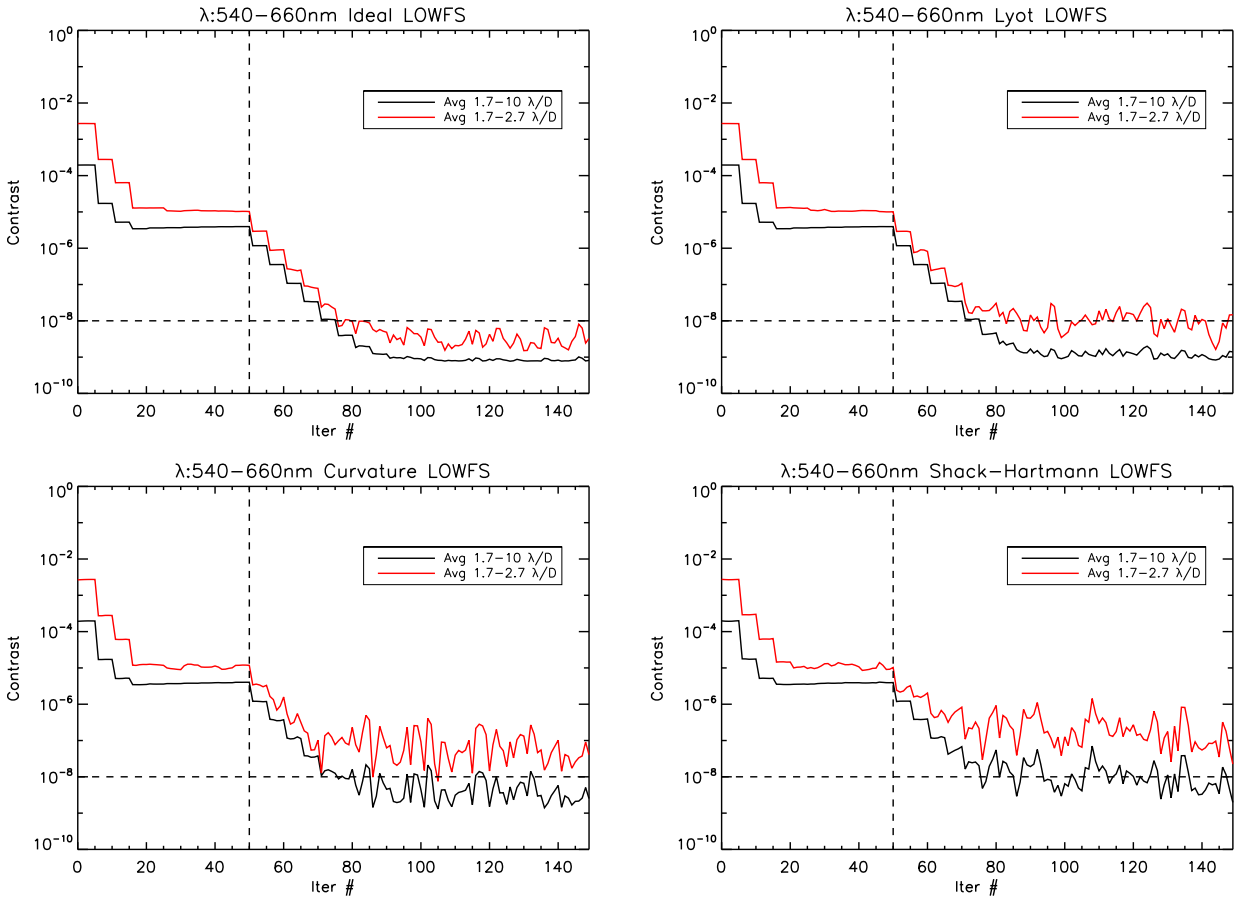

Figure 12: Dark zone convergence for end-to-end PROPER simulations of the entire optical system (telescope to science detector) with LOWC and EFC running simultaneously. These simulations are for ϵ Eri (V=3.73, K2V). Top-left: Ideal LOWFS, top-right: Lyot LOWFS, bottom-left: curvature LOWFS, bottom-right: Shack-Hartmann LOWFS. The red lines show the average dark zone contrast between 1.7-2.7 λ/D. The black lines show the average contrast across the entire dark zone (1.7-10 λ/D). The vertical dashed line shows the point where the system transitions from correcting only phase to correcting both phase and amplitude using EFC. The LOWC system based on the Lyot LOWFS is the only one capable of reaching 10^{-8}.

sensitivity to higher order modes. This may be an acceptable trade given that control of the highest order modes is not required – as this work has shown. Example contrast maps for the Lyot system are shown in Figure 11.

5. CONCLUSIONS

It has been shown that a Lyot LOWFS is the only reasonable choice to meet the design goals of the PICTURE-C mission. This sensor will be selected going forward. An additional tip-tilt sensor may be used in the blue channel to provide additional feedback to the control system and larger dynamic range during target acquisition. Hybrid systems such as a 400 Hz tip-tilt sensor in the blue channel and a 50 Hz Lyot sensor in the science band were also shown to perform well and may be considered as backup options. Since this sensor design is specific to the VVC, it is incompatible with the visible nulling coronagraph (VNC) planned for use in flight 1.[16] Either the Shack-Hartmann or the curvature sensor could easily be adapted to take the place of the tip-tilt sensor in that design, which also sits in a secondary blue channel. Both provide enough performance to reach the nuller limit of 10^{-4}. A possible path forward is to choose one blue channel sensor for both flights and add the Lyot sensor for higher performance in the second flight.

ACKNOWLEDGMENTS

This work was funded under NASA grant NNX15AG23G S01. Thanks to Jim Lanzi and David Stuchlik at WFF for providing the WASP test flight 2 data.

REFERENCES

[1] Mawet, D., Serabyn, E., Moody, D., Kern, B., Niessner, A., Kuhnert, A., Shemo, D., Chipman, R., McClain, S., and Trauger, J., "Recent results of the second generation of vector vortex coronagraphs on the high-contrast imaging testbed at jpl," *Proc. SPIE* **8151**, 81511D (2011).

[2] http://www.northropgrumman.com/businessventures/aoaxinetics/Pages/default.aspx. AOA Xinetics website.

[3] Krist, J. E., "Proper: an optical propagation library for idl," *Proc. SPIE* **6675**, 0 (2007).

[4] http://exep.jpl.nasa.gov/technology/. NASA TDEM website.

[5] Krist, J. E., Moody, D. C., Mawet, D., Trauger, J. T., Belikov, R., Shaklan, S. B., Guyon, O., and Vanderbei, R. J., "End-to-end simulations of different coronagraphic techniques," *Proc. SPIE* **7440**, 16 (2009).

[6] Mawet, D., Pueyo, L., Moody, D., Krist, J., and Serabyn, E., "The vector vortex coronagraph: sensitivity to central obscuration, low-order aberrations, chromaticism, and polarization," *Proc. SPIE* **7739**, 14 (2010).

[7] http://sites.wff.nasa.gov/code820/technology_wasp_details.html. WASP website.

[8] Mendillo, C. B., Chakrabarti, S., Cook, T. A., Hicks, B. A., and Lane, B. F., "Flight demonstration of a milliarcsecond pointing system for direct exoplanet imaging," *Appl. Opt.* **51**, 7069–7079 (2012).

[9] Trauger, J., Moody, D., Gordon, B., Krist, J., and Mawet, D., "A hybrid lyot coronagraph for the direct imaging and spectroscopy of exoplanet systems: recent results and prospects," *Proc. SPIE* **8151**, 81510G (2011).

[10] Guyon, O., Matsuo, T., and Angel, R., "Coronagraphic low-order wave-front sensor: Principle and application to a phase-induced amplitude coronagraph," *ApJ* **693**, 75–84 (2009).

[11] Singh, G., Martinache, F., Baudoz, P., Guyon, O., Matsuo, T., Jovanovic, N., and Clergeon, C., "Lyot-based low order wavefront sensor for phase-mask coronagraphs: Principle, simulations and laboratory experiments," *PASP* **126**, 586–594 (2014).

[12] www.e2v.com. e2v website.

[13] www.astro-cam.com. Astronomical Research Cameras (ARC) website.

[14] Castelli, F. and Kurucz, R. L., "New grids of atlas9 model atmospheres," *IAU Symp.* **Poster A20** (2003).

[15] Give'on, A., Kern, B., Shaklan, S., Moody, D. C., and Pueyo, L., "Broadband wavefront correction algorithm for high-contrast imaging systems," *Proc. SPIE* **6691** (2007).

[16] Mendillo, C. B., Hicks, B. A., Cook, T. A., Bifano, T. G., Content, D. A., Lane, B. F., Levine, B. M., Rabin, D., Rao, S. R., Samuele, R., Schmidtlin, E., Shao, M., Wallace, J. K., and Chakrabarti, S., "Picture: a sounding rocket experiment for direct imaging of an extrasolar planetary environment," *Proc. SPIE* **8442** (2012).